Inorganic Chemistry
Article
pubs.acs.org/IC

Tuning the Photophysical Properties of *anti*-$B_{18}H_{22}$: Efficient Intersystem Crossing between Excited Singlet and Triplet States in New 4,4′-$(HS)_2$-*anti*-$B_{18}H_{20}$.

Vicenta Saurí,[§] Josep M. Oliva,*[‡] Drahomír Hnyk,[†] Jonathan Bould,[†] Jakub Braborec,[†,⊗] Manuela Merchán,[§] Pavel Kubát,[‖] Ivana Císařová,[⊥] Kamil Lang,*[†] and Michael G. S. Londesborough*[†]

[†]Institute of Inorganic Chemistry of the AS CR, v.v.i., 250 68 Husinec-Řež, Czech Republic
[‡]Instituto de Química-Física "Rocasolano", Consejo Superior de Investigaciones Científicas, ES-28006 Madrid, Spain
[§]Instituto de Ciencia Molecular, Universidad de Valencia, E-46980 Paterna, Valencia, Spain
[‖]J. Heyrovský Institute of Physical Chemistry of the AS CR, v.v.i., Dolejškova 3, 182 23 Praha 8, Czech Republic
[⊥]Faculty of Sciences, Charles University in Prague, 2030 Hlavova, 128 43 Praha 2, Czech Republic
[⊗]Faculty of Science, J. E. Purkyně University in Ústí nad Labem, 400 96 Ústí nad Labem, Czech Republic

Supporting Information

ABSTRACT: The tuning of the photophysical properties of the highly fluorescent boron hydride cluster *anti*-$B_{18}H_{22}$ (**1**), by straightforward chemical substitution to produce 4,4′-$(HS)_2$-*anti*-$B_{18}H_{20}$ (**2**), facilitates intersystem crossing from excited singlet states to a triplet manifold. This subsequently enhances $O_2(^1\Delta_g)$ singlet oxygen production from a quantum yield of $\Phi_\Delta \sim 0.008$ in **1** to 0.59 in **2**. This paper describes the synthesis and full structural characterization of the new compound 4,4′-$(HS)_2$-*anti*-$B_{18}H_{20}$ (**2**) and uses UV−vis spectroscopy coupled with density functional theory (DFT) and ab initio computational studies to delineate and explain its photophysical properties.

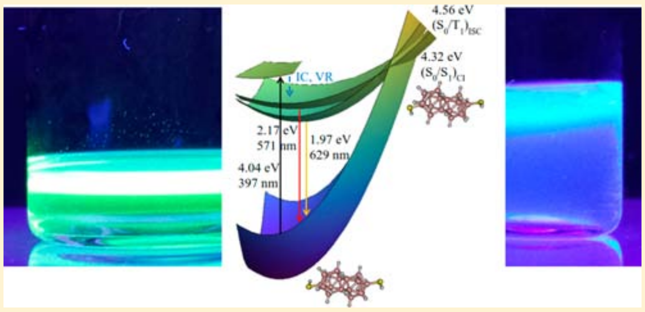

■ INTRODUCTION

We have recently become interested in the chemistry and properties of the boron hydride octadecaborane(22), $B_{18}H_{22}$. This compound, which exists as two isomers, *anti*-$B_{18}H_{22}$ and *syn*-$B_{18}H_{22}$, has become relevant to the semiconductor industry as a boron dopant of silicon.[1] Its commercial importance has kindled research activity into the synthesis of octadecaborane(22) and aspects of its chemistry. In this wider context, we have recently published work describing a conversion route between the two isomers of octadecaborane(22) via their common $[B_{19}H_{22}]^-$ anion,[2] together with a thorough treatise on the fluorescence of *anti*-$B_{18}H_{22}$, and a rationalization of why the *syn*-$B_{18}H_{22}$ isomer does not share the same photophysical property.[3] Although some pyridine derivatives of other cluster boranes and carboranes have been reported to be luminescent under UV irradiation,[4] the high quantum yield fluorescence ($\Phi_F = 0.97$) seen for *anti*-$B_{18}H_{22}$ is unique among the neutral binary boron hydrides. In addition to fluorescence, the production of $O_2(^1\Delta_g)$ singlet oxygen via an energy transfer process from a lowly populated triplet manifold ($\Phi_\Delta = 0.008$ in hexane solutions) was also observed.[3] Density Functional Theory (DFT) and ab initio calculated Potential Energy Hypersurface (PEH) minima and crossings for *anti*-$B_{18}H_{22}$ showed that all its triplet states lie, in terms of their relative energies, far from the S_1 state minimum, thus making intersystem crossing (ISC) to triplet states highly unlikely at this point (see Figure 1). This finding is significant as S_1 state minimum structures are usually the most favorable for ISC as energy is trapped there for a sufficient time for such processes

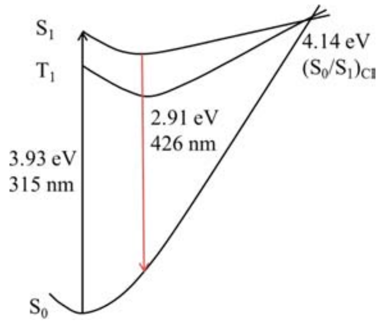

Figure 1. DFT and ab initio calculated PEH minima and crossings for *anti*-$B_{18}H_{22}$ (**1**). (See reference 3 for full calculational and experimental data).

Received: February 27, 2013
Published: July 26, 2013

to occur. This is not the case for the *anti*-$B_{18}H_{22}$ system, which, instead, sees the S_1-T_1 energy gap decreasing as it approaches the (S_0/S_1) conical intersection point along the PEH surface (see Figure 1), making this point the most likely for ISC to occur. That the (S_0/S_1) conical intersection crossing is so high in energy relative to the S_1 state minimum is, essentially, the reason that *anti*-$B_{18}H_{22}$ overwhelmingly favors fluorescence rather than ISC and the subsequent formation of $O_2(^1\Delta_g)$ singlet oxygen.[3] However, these observations do evoke the question: Could the latter S_1-T_1 quantum hop be facilitated, and the molecule induced into producing singlet oxygen more efficiently?

Here we report on how a one-step chemical modification of *anti*-$B_{18}H_{22}$ (**1**), by thiolation, to produce 4,4′-$(HS)_2$-*anti*-$B_{18}H_{20}$ (**2**), can be used to significantly increase the probability of ISC between S_1 and T_1 states and thus promote a more efficient production of $O_2(^1\Delta_g)$ in oxygen saturated cyclohexane solutions ($\Phi_\Delta = 0.59$). This contribution describes the synthesis and full structural characterization of 4,4′-$(HS)_2$-*anti*-$B_{18}H_{20}$ (**2**) and uses UV−vis spectroscopy coupled with DFT and ab initio computational studies to delineate and explain its photophysical properties.

■ RESULTS AND DISCUSSION

Synthesis and Structural Characterization of 4,4′-$(HS)_2$-*anti*-$B_{18}H_{20}$ (2) by Single-Crystal X-ray Crystallography, NMR Spectroscopy, and Mass Spectrometry. Our previous computational study[3] on the photophysics of *anti*-$B_{18}H_{22}$ indicates that the additional energy this molecule receives after irradiation is distributed over a number of molecular vibrational modes, or interboron connectivities, as it moves along the PEH from its S_1 minimum toward the (S_0/S_1) conical intersection point. Significantly, during the PEH range in which the probability for S_1-T_1 ISC to occur is increasing, the geometry of the molecule remains essentially unchanged with the exception of the elongation of three B-B connectivities and the contraction of one.[3] This situation guided our thinking when considering what chemical change to the *anti*-$B_{18}H_{22}$ might maximize the probability of ISC between S_1-T_1 states, that is, a molecular modification in which the eighteen-vertex geometry in compound **1** would be essentially preserved. A survey of the literature, however, revealed that the great majority of known derivatives of **1** have significant alterations in the overall cluster molecular geometry, and are very often with additional or fewer vertices.[24] Accordingly, we chose to take advantage of a well-recognized synthetic procedure that has been used with several other boron hydride species while producing only small changes in their molecular geometries, namely, cluster thiolation.[15]

Thus, the heating of *anti*-$B_{18}H_{22}$ with a 10-fold excess of elemental sulfur and $AlCl_3$ in a sealed glass tube gave the new compound 4,4′-$(HS)_2$-*anti*-$B_{18}H_{20}$ (**2**) in yields of up to 80%. Single-crystals suitable for single-crystal X-ray diffraction were grown from the slow cooling of a saturated hot cyclohexane/benzene solution. Figure 2 shows the molecular structure of the resultant benzene solvate of 4,4′-$(HS)_2$-*anti*-$B_{18}H_{20}$ (**2**). All cluster hydrogen atoms were apparent in the residual electron-density map after anisotropic refinement of the heavier atoms. For the thiol hydrogen atoms, the remaining highest electron-density peak, after isotropic hydrogen refinement, was in a reasonable position close to the sulfur atoms, but final refinement was carried out using a riding model.

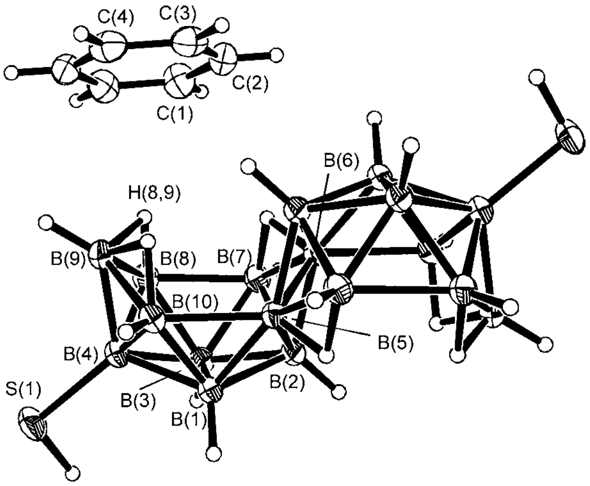

Figure 2. Crystallographically determined molecular structure of the benzene cocrystallite of 4,4′-$(HS)_2$-*anti*-$B_{18}H_{20}$ (**2**).

The centroid of the cocrystallized benzene ring in the asymmetric unit of **2** is located over the H(8,9) bridging hydrogen atom of the borane cluster. This hydrogen-bonding-type of interaction with aromatic solvents,[16] first observed by Gibb and Kennedy,[17] has also been seen in the benzene solvate of *anti*-$B_{18}H_{22}$ itself.[18] Its presence in **2** may be taken as an indication that π-acidity of the H(8,9) bridging hydrogen atom is not substantially altered by the presence of the thiol substituents. Indeed, the overall eighteen-vertex cluster geometry of **1** is undisturbed in the thiolated compound **2**, and a comparison of the interatomic dimensions for compounds **1** and **2** (Table 1 shows selected B-B connectivity lengths for solvated compounds **1** and **2**) confirms that the molecular structure does not undergo a substantial change in its

Table 1. Selected B-B Connectivity Lengths [Å] for 4,4′-$(HS)_2$-*anti*-$B_{18}H_{20}$·C_6H_6 (2·C_6H_6) with Comparison Data for *anti*-$B_{18}H_{22}$·C_6H_6 (1·C_6H_6)[18]

	1·C_6H_6	**2**·C_6H_6	diff.
B(1)−B(10)	1.740(5)	1.7566(18)	+0.017
B(1)−B(5)	1.746(5)	1.7564(17)	+0.010
B(1)−B(3)	1.778(5)	1.7920(18)	+0.014
B(1)−B(2)	1.786(5)	1.7934(18)	+0.007
B(2)−B(3)	1.746(5)	1.7590(17)	+0.013
B(1)−B(4)	1.786(5)	1.7994(17)	+0.013
B(2)−B(7)	1.774(5)	1.7943(18)	+0.020
B(2)−B(5^a)	1.765(4)	1.7620(18)	−0.003
B(3)−B(8)	1.723(6)	1.7497(18)	+0.027
B(3)−B(7)	1.746(5)	1.7596(18)	+0.014
B(3)−B(4)	1.774(5)	1.7839(18)	+0.010
B(4)−B(9)	1.702(5)	1.7264(18)	+0.024
B(4)−B(10)	1.775(5)	1.7905(18)	+0.016
B(4)−B(8)	1.789(5)	1.8136(19)	+0.025
B(4)−S(1)		1.8690(12)	
B(5)−B(5^a)	1.805(6)	1.801(2)	−0.004
B(5)−B(7^a)	1.815(5)	1.8192(17)	+0.004
B(5)−B(10)	1.968(5)	1.9741(17)	+0.006
B(7)−B(8)	1.946(5)	1.9649(18)	+0.019
B(8)−B(9)	1.795(5)	1.8004(18)	+0.005
B(9)−B(10)	1.783(5)	1.7792(19)	−0.004

[a] Equivalent symmetry related atoms.

interatomic separations because of the presence of the thiol substituents. Most of the differences between the distances are just within three standard uncertainties, although almost all are in the direction of being longer than the unsubstituted cluster. There is a consistent lengthening of B-B connectivities associated with the substituted cluster atom B(4), but this is small at about 0.02 Å. Indeed, most of the differences between unsubstituted **1** and thiolated **2** are of a similar magnitude to those between solvated and unsolvated *anti*-$B_{18}H_{22}$.[18]

It is of interest and of synthetic utility that the synthesis of compound **2** produced no significant amounts of any other thiolated boron hydride cluster species as is found in the analogous reaction of the geometrically related smaller cluster boron hydride, *nido*-$B_{10}H_{14}$ ($B_{18}H_{22}$ may be regarded as two *nido*-$B_{10}H_{14}$ clusters fused by a common edge). Reaction of *nido*-$B_{10}H_{14}$ with $AlCl_3$ and sulfur affords three products; two monosubstituted isomers, 1-(HS)-*nido*-$B_{10}H_{13}$ (**3**) and 2-(HS)-*nido*-$B_{10}H_{13}$ (**4**), and a disubstituted derivative, 1,2-$(HS)_2$-*nido*-$B_{10}H_{12}$ (**5**).[15] Compound **2** is clearly related to 2-(HS)-*nido*-$B_{10}H_{13}$, with the thiol groups positioned on equivalent basal vertices (atomic positions 2 and 4 are equivalent in decaborane), but, despite repeated experimentation, no evidence was found for any substantial generation of $\{B_{18}H_x\}$ equivalents of compounds **3** and **5**. Indeed, only when thiolation of **1** was conducted using molar equivalents of elemental sulfur and $AlCl_3$ were small amounts of an asymmetrical species in the crude product mix detected by NMR spectroscopy. Mass spectrometry indicated it to be a monosubstituted $B_{18}H_{21}(SH)$ species, but unfortunately no crystallographic data were obtained to confirm this empirical formula or identify the location of the cluster substitution. This observation aside, the major reaction product in this experiment was still compound **2**.

Multinuclear NMR spectroscopic experiments confirmed that the solution-phase structure of compound **2** is consistent with that of the crystallographically determined structure (Figure 2). Table 2 lists all ^{11}B and ^{1}H measured chemical shifts, along with their cluster assignments, as well as GIAO-B3LYP/II-calculated ^{11}B NMR shielding data, using a B3LYP/6−31+G* optimized geometry. [We are aware that GIAO-MP2-based computed shielding tensors are by far the most accurate for comparing experimental and computed NMR chemical shifts. This is particularly so for small, structurally strained boranes (the effect of dynamic electron correlation is even unavoidable in such systems) and heteroboranes, see Hnyk, D.; Jayasree, E.G. *J. Comput. Chem.* **2012**, *34* (8), 656−661, and references therein. However, such calculations are excessively CPU and RAM demanding procedures for systems as large as **2**]. The measured ^{11}B NMR spectrum shows nine resonances, consistent with the C_i symmetry of the molecule. Two of the resonances are singlets: one for the subcluster-conjoining B(5,6) pair and one for the −SH substituted B(4,4′) pair.

Table 2. Experimentally Measured ^{11}B and ^{1}H NMR Chemical Shift Data and GIAO-B3LYP ^{11}B NMR Data for 4,4′-$(HS)_2$-*anti*-$B_{18}H_{20}$ 2.

assignment[a]	δ (^{11}B)/ppm[b,c]	δ(^{1}H)/ppm[b]
3	+15.0 [+15.6]	+4.07
10	+8.9 [+9.9]	+4.33
5[d]	+2.5 [+2.7]	
9	+2.1 [+1.2]	+3.68
1	+0.7 [+0.4]	+3.26
8	−4.0 [-6.6]	+3.31
7	−12.9 [−15.9]	+3.03
4	−30.1 [−30.0]	
2	−32.3 [−36.2]	+0.06
S-H		+0.10
μH(9,10)		+0.01
μH(6,7)		−0.87
μH(8,9)		−2.18

[a] Based on two-dimensional [^{11}B-^{11}B] and [^{1}H-^{1}H] COSY and ^{1}H-{^{11}B selective} NMR experiments and comparison to published data for compound 1.[19] [b] In $CDCl_3$ solution at 294 K. [c] GIAO/II//B3LYP/6−31+G* ^{11}B NMR data in square brackets. [d] Equivalent to B(6) by C_i molecular symmetry.

Figure 3 shows a comparison of the measured ^{11}B-{^{1}H} NMR spectra of compounds **1** and **2**. As might be expected, because of the very similar 18-vertex boron cluster geometry and symmetry, the two spectra are very alike. There are small upfield shifts for B(5,6) and B(9,9′) and a considerable shift to low field for the B(4,4′) resonance of some 9.6 ppm. This latter observation may be expected as it is the B(4,4′) atomic positions that are thiol-substituted. Indeed, a similarity may be found with the SH substitution of icosahedral $[B_{12}H_{12}]^{2-}$ (giving $[1\text{-}(HS)\text{-}B_{12}H_{11}]^{2-}$) that results in a downfield chemical shift of the HS-substituted boron atom resonance by about 6.4 ppm compared to the equivalent B atom resonance in the parent $[B_{12}H_{12}]^{2-}$.[20]

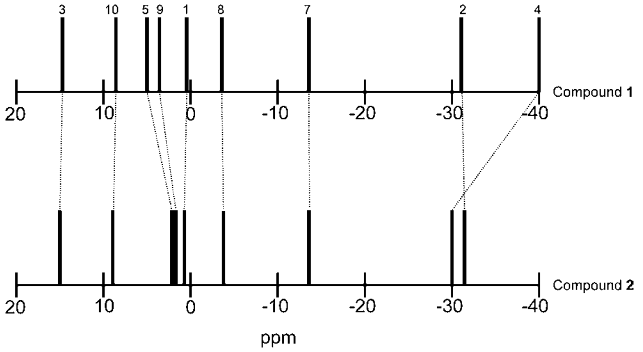

Figure 3. Comparison of the measured ^{11}B-{^{1}H} NMR spectra of *anti*-$B_{18}H_{20}$ **1** and 4,4′-$(HS)_2$-*anti*-$B_{18}H_{20}$ **2**.

Selective ^{1}H-{^{11}B} irradiation of the singlet boron resonance associated with the thiol-substituted B(4,4′) vertices resulted in a clear sharpening of the thiol proton resonance (+ 0.10 ppm) by the removal of the $^{2}J(^{11}B\text{-}S\text{-}^{1}H)$ coupling, enabling the definitive identification and assignment of the thiol proton. It may be noted that the measured chemical shift of the thiol proton in compound **2** (+ 0.10 ppm) is very similar to that for the thiol proton in the structurally related 2-(HS)-*nido*-$B_{10}H_{13}$ (**4**) (+ 0.12 ppm).

Electrospray Ionization Mass spectrometry measurements for compound **2** consistently gave spectra of a single boron hydride cluster species with a typical boron mass envelope and cutoff point at m/z 283. This value is consistent with an empirical formula $[^{11}B_{18}{}^{1}H_{21}{}^{32}S_2]^-$ for deprotonated compound **2**. Evidence of the thermal stability of **2** came from attempts to measure its melting point. In the Supporting Information there is a filmed melting-point experiment for **2**. Samples of the compound were heated at a rate of 10 °C min^{-1} in an inert argon atmosphere up to a maximum of 400 °C. Even at 400 °C, no melting occurred (cf. melting point of *anti*-$B_{18}H_{22}$ of 179−180 °C) although, while in the temperature range 250−270 °C, a color change from yellow to orange was observed. This property is currently the subject of a further investigation on which we hope to report later. Nevertheless, with the target compound **2** produced in good yield and structurally characterized, our focus turned to its photophysical properties.

Experimental and Computational Investigation of the Photophysical Properties of 4,4′-$(HS)_2$-*anti*-$B_{18}H_{20}$ (2). The following discussion is divided into two sections, the first on the absorption properties and the second on the emission of energy together with the geometrical changes that occur during these transitions.

Absorption. The CASSCF/CASPT2 (Complete Active Space Self-Consistent Field, Complete Active Space Perturbation Theory: see Supporting Information for additional information about this method) calculated absorption profile and the experimentally determined absorption spectrum of **2** are compiled in the Supporting Information, Table S1, and Figure 4a, respectively. The ground-state geometry for S_0, optimized at the B3LYP level and imposing a C_i symmetry constraint, labeled 1^1A_g, was used in the computation of the absorption spectrum of **2**. Single photon allowed transitions were calculated at the ground-state equilibrium structure up to 225 nm (5.50 eV). The majority of these calculated transitions are in the range of the experimental data recorded in cyclohexane up to 240 nm. The main molecular orbitals (MOs) as HOMO- (H) and LUMO-like (L) orbitals were identified by means of the occupation number of the corresponding CASSCF natural orbitals (NOs); the MO labels are shown in Figure 5.

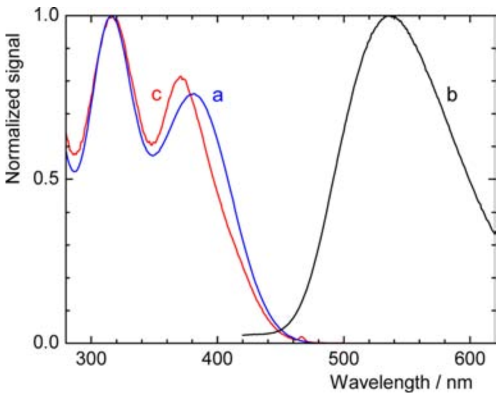

Figure 4. Normalized absorption (a) and fluorescence emission (b) spectra of **2** in air-saturated cyclohexane compared with the fluorescence excitation spectrum (c).

The lowest-energy singlet−singlet transition $1^1A_g \rightarrow 1^1A_u$, described at the CASSCF level as the H → L one-electron promotion with a weight of 85% (see Supporting Information, Table S1), is computed vertically at 396 nm (3.13 eV), with an oscillator strength of 0.065 and can be assigned to the lowest-intensity band maximum observed for **2** at 381 nm (3.25 eV). A second transition, to the 2^1A_u state, is computed at 307 nm (4.04 eV), described essentially by the configuration H-2 → L (79%), having a computed oscillator strength of 0.196. This transition can be assigned to the observed peak at 316 nm (3.92 eV) in the measured absorption spectrum of **2**. With the exception of one other weak transition to 3^1A_u, computed at 257 nm (4.83 eV), which lies beneath the most intense band measured at 240 nm (5.17 eV), only one other allowed transition is predicted within the range of the experimental spectrum. This transition, at 247 nm (5.02 eV), with a large associated oscillator strength (0.528), corresponds to the 4^1A_u state and can be assigned to the most intense band in the absorption spectrum of **2**.

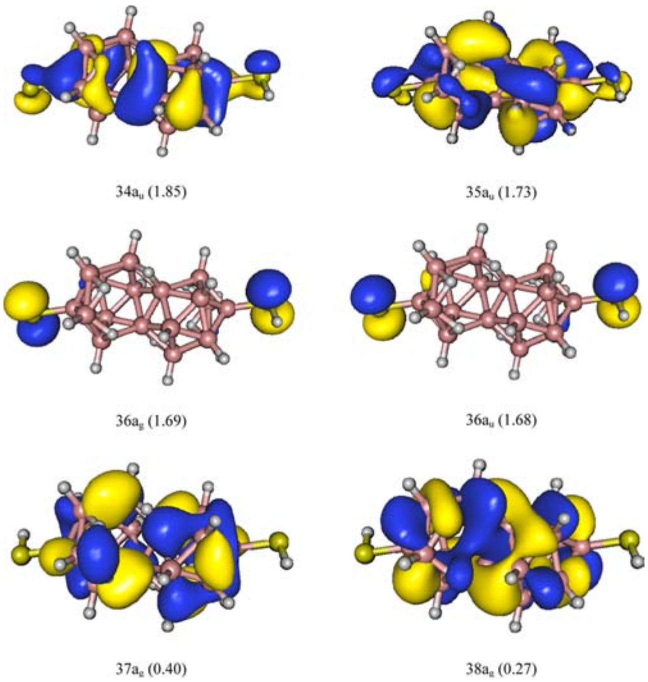

Figure 5. Most relevant CASSCF natural orbitals for **2**. The MOs are named as H, H-1, H-2, H-3, L, and L+1 for $36a_u$, $36a_g$, $35a_u$, $34a_u$, $37a_g$, and $38a_g$, respectively. Occupation numbers within parentheses.

Supporting Information, Table S1 also contains calculated triplet states of A_g and A_u symmetry for the energy range 410−238 nm (3.02−5.20 eV). The lowest singlet−triplet transition results in the population of the 1^3A_u state at 410 nm (3.02 eV) described by mainly two configurations: H → L (47%) and H-2 → L (41%). It should be noted that, because of the low energy difference between 1^1A_u and 1^3A_u states of 0.11 eV, and a relatively high spin−orbit coupling (SOC) of 2.92 cm^{-1}, an efficient ISC process is to be expected to occur at the ground-state Franck−Condon (FC) region.

Emission. Table 3, Figure 4b and Figure 6 summarize the proposed photophysics based on our experimental and computed results. The brightest state does not correspond to the lowest-lying singlet excited state 1^1A_u as it does for *anti*-$B_{18}H_{22}$.[3] Rather, in the low-energy range, it is the transition to a S_3 state, labeled 2^1A_u, which has the most significant oscillator strength (0.196). We therefore conclude that initial excitation results in promotion to the S_3 state followed by decay to the S_1 state (1^1A_u) through vibrational relaxation and internal conversion within a femtosecond time scale. Once the system reaches the S_1 energy minimum two possible outcomes dominate. The first of these is ISC to, and population of, a triplet manifold, which is possible because the energy difference between S_1 and T_1 is a relatively small 0.14 eV, with a computed SOC of 3.37 cm^{-1}. These values are similar to those calculated at the FC region: $\Delta E(S_1\text{-}T_1) = 0.11$ eV and SOC of 2.97 cm^{-1}. ISC processes are therefore likely in these two regions of the PEH. The second most possible outcome is a fluorescence emission, computed at 571 nm (2.17 eV) and

Table 3. Theoretical (CASPT2) Absorption and Emission Spectra of 2 Compared with the Experimental Data in Cyclohexane

				CASPT2						
state	$E_{VA}{}^{a}$ /eV	$\lambda_{VA}{}^{a}$ /nm	f	$E_{VE}{}^{a}$ /eV	$\lambda_{VE}{}^{a}$ /nm	$T_e{}^{a}$ /eV	$\lambda_e{}^{a}$ /nm	$E_{TT}{}^{a}$ /eV	$\lambda_{TT}{}^{a}$ /nm	τ^{0a}/s
1^1A_g										
1^1A_u	3.13	396	0.065	2.17	571	2.78	444			1.09×10^{-7}
2^1A_g	3.27	379								
2^1A_u	4.04	307	0.196							
1^3A_u	3.02	410		1.97	629	2.61	475			1.69×10^{-3}
$1^3A_u \rightarrow 2^3A_g$			0.210^{d}					1.90	653	
				Experimental						
	$A_{max}{}^{b}$ /eV	$\lambda_{amax}{}^{b}$ /nm		$E_{max}{}^{b}$ /eV	$\lambda_{emax}{}^{b}$ /nm	$E_T{}^{b}$ /eV	$\lambda_T{}^{b}$ /nm	$E_{TT}{}^{b}$ /eV	$\lambda_{TT}{}^{b}$ /nm	$\tau_F{}^{b}$/s
1^1A_u	3.25	381		2.31	536					0.94×10^{-9}
2^1A_u	3.92	316								
1^3A_u						2.08	596			$\tau_T/s = (1.4 \times 10^{-5})^{c}$
$1^3A_u \rightarrow 2^3A_g$								1.91	648	

[a] Computed vertical absorption energy (E_{VA}) and wavelength (λ_{VA}), vertical emission energy (E_{VE}) and wavelength (λ_{VE}), electronic band origin energy (T_e) and wavelength (λ_e), triplet−triplet absorption energy (E_{TT}) and wavelength (λ_{TT}), and natural radiative lifetime (τ^0). [b] Experimental absorption band maxima energy (A_{max}) and wavelength (λ_{amax}), fluorescence band maximum energy (E_{max}) and wavelength (λ_{emax}), phosphorescence band maximum energy (E_T) and wavelength (λ_{TT}), maximum of the triplet−triplet absorption energy (E_{TT}) and wavelength (λ_T), and fluorescence lifetime (τ_F). [c] Lifetime of the triplet states (τ_T) measured in argon-saturated cyclohexane. [d] Corresponds to this electronic transition at the lowest triplet T_1 optimized geometry. The value $f = 0.128$ (reported in Supporting Information, Table S1) is related to $1^3A_u \rightarrow 2^3A_g$ electronic transition at the ground-state S_0 optimized geometry.

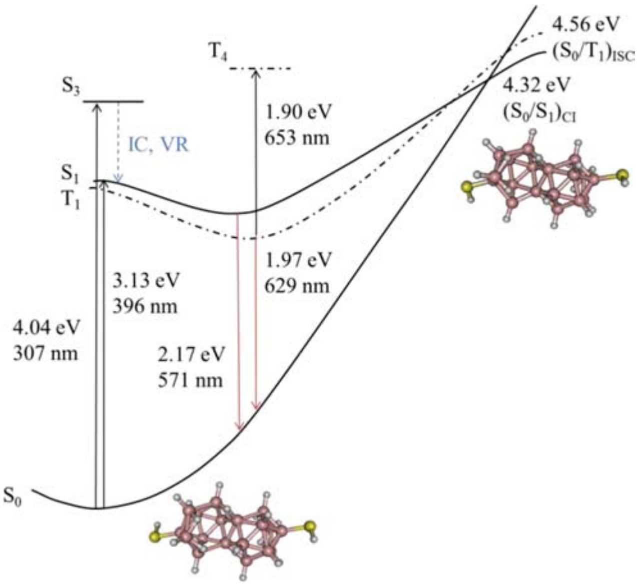

Figure 6. Photophysics, PEHs, and structures of the ground state (S_0), lowest-energy excited singlet state (S_1) and lowest-energy excited triplet state (T_1) for **2** based on the CASPT2 calculated data (see Table 3 for full calculated and experimental data).

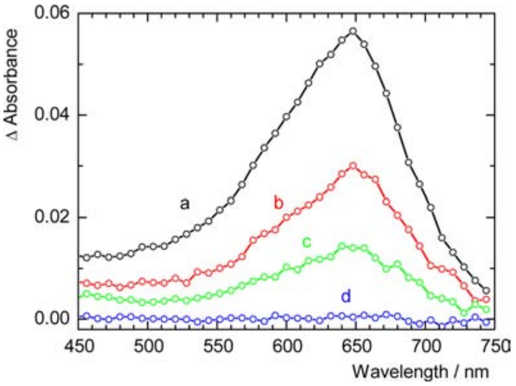

Figure 7. Transient absorption spectra of **2** (133 μM in cyclohexane) at 2 (a), 5 (b), 10 (c), and 50 (d) μs after excitation. Excited at 308 nm.

measured experimentally at 536 nm (2.31 eV). The presence of a minimum along the main decay pathway of the S_1 state (Figure 6) is characteristic of the partially emissive character of **2**. Fluorescence was measured experimentally to have a relatively short lifetime (0.94 ns), which indicates competition between fluorescent and nonradiation processes such as ISC to populate the lowest-energy triplet manifold.

The formation of the triplet states has been monitored experimentally by transient absorption and time-resolved phosphorescence. In contrast to *anti*-$B_{18}H_{22}$ **1**, which has no transient absorption in a microsecond time scale (the quantum yield of the triplet states was estimated to be less than 0.03), we have observed the transient absorption of **2** (Figure 7). These long-lived transients can be attributed to triplet states because they are quenched effectively by oxygen. Measurements in oxygen-, air-, and argon-saturated solutions enabled the full characterization of the triplet states (Table 3). In addition, time-resolved luminescence experiments revealed two types of emissions: (i) ns-emission that is not affected by oxygen and is attributed to the above-discussed fluorescence (Figures 4b and 8); (ii) slow microsecond emission (Figure 8) that is strongly quenched by oxygen and decays with the same rate as the triplet states measured by transient absorption spectroscopy (see Supporting Information, Figure S7). Therefore, the luminescence emission spectrum with a maximum at 596 nm (2.08 eV) can be assigned to phosphorescence. This calculated transition is found at 629 nm (1.97 eV). Moreover, the fluorescence excitation spectrum of **2** does not match the absorption band at 381 nm (Figure 4) which supports the proposition that efficient ISC to triplet states occurs at the ground-state FC region as mentioned in the discussion above.

Time-resolved absorption spectroscopy in argon-saturated cyclohexane has estimated the lifetime of the triplet state at 14

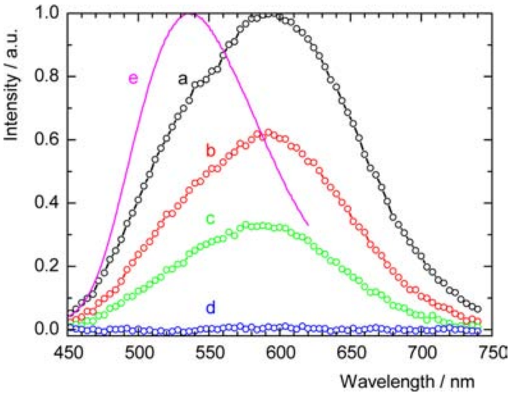

Figure 8. Comparison of the phosphorescence spectra of **2** (133 μM) in argon-saturated cyclohexane at 2 (a), 5 (b), 10 (c), and 50 (d) μs after excitation with the normalized fluorescence spectrum in the nanosecond time scale (e). Excited at 308 nm.

μs, characterized by a phosphorescence band maximum at 596 nm (2.08 eV) (Figures 7 and 8). In general, the triplet states are quenched due to the production of $O_2(^1\Delta_g)$ in the presence of molecular oxygen when the energy of the donor is higher than the 0.97 eV required to populate the O_2 $(^1\Delta_g)$ state through a triplet−triplet energy transfer (TET) mechanism.[21,22] In this case, the computed adiabatic energy for T_1 of the **2** donor is 475 nm (2.61 eV), exceeding the 0.97 eV needed for O_2 $(^1\Delta_g)$ formation. When the triplet donor lies higher in energy than the final acceptor state, the TET process is exothermic and diffusion controlled with molecular oxygen behaving as a rigid, classical acceptor.[23]

To assess the efficiency of the $O_2(^1\Delta_g)$ formation by **2**, we recorded the luminescence of $O_2(^1\Delta_g)$ at 1270 nm upon pulsed laser excitation. In general, the measured signals reflect the lifetimes of the parent triplet states and of $O_2(^1\Delta_g)$ in a given solvent. Because the lifetimes of the triplet states in the presence of oxygen are short (<1 μs), the obtained signals are well fitted by a monoexponential function and correspond to the lifetime of $O_2(^1\Delta_g)$ in cyclohexane (see Supporting Information, Figure S8). The quantum yield of the singlet oxygen formation, Φ_Δ, for compound **2** in air-saturated cyclohexane solution, is 0.59. This value constitutes an important enhancement of $O_2(^1\Delta_g)$ production with respect to *anti*-$B_{18}H_{22}$ (**1**) ($\Phi_\Delta \sim 0.008$)[3] and is a value comparable to those of typical sensitizers such as porphyrins and phthalocyanines.[22] Comparison of the measured $O_2(^1\Delta_g)$ lifetimes for **2** in cyclohexane solutions (τ_Δ = 24 μs) with literature data for pure cyclohexane (τ_Δ = 24 μs)[25] indicates that $O_2(^1\Delta_g)$ does not interact with the cluster.

Our CASPT2//CASSCF calculations have estimated the lowest-lying $(S_0/S_1)_{CI}$ energy crossings adiabatically at 4.32 eV (Figure 6). The energy barrier found between the S_1 energy minimum and the $(S_0/S_1)_{CI}$ is a prohibitively large 1.54 eV, making this structure, in an analogy to the case of **1**, highly unlikely to contribute to the relaxation of the **2** system. Furthermore, the CASPT2//CASSCF computations have found the lowest-energy $(S_0/T_1)_{ISC}$ crossing adiabatically to be at 4.56 eV. The energy barrier between the T_1 minimum energy and the $(S_0/T_1)_{ISC}$ is thus estimated to be 1.95 eV. These relatively large energy barriers make the population of T_1 via ISC from the S_1 energy minimum, at which point the S_1-T_1 energy difference is only 0.14 eV, very probable and subsequent phosphorescence or alternatively fluorescence highly likely. This consideration based on CASPT2//CASSCF calculations supports the observed photophysics of the system described above.

Geometrical Changes at the Stationary Points of the PEH. To obtain a complete energy profile of the photophysics of **2**, the CIs and ISCs of the low-lying states along with the ground state S_0 have been computed as MECPs (Minimum Energy Crossing Points). The two-dimensional PEHs of the S_0, S_1, and T_1 states for 4,4′-$(HS)_2$-*anti*-$B_{18}H_{20}$ (**2**) are depicted in Figure 6. It is worth mentioning that the reaction coordinate is different for S_1 (solid line) and T_1 states (dashed line). In the former, the change in molecular geometry mainly corresponds to the elongation of the B(8)-B(9) or B(8′)-B(9′) connectivities (see Figure 2 for cluster numbering) together with a rotation of the thiol group (dihedral angle ∠B(1)-B(4)-SH or ∠B(1′)-B(4′)-SH′) of 80.2°. For the T_1 state, the reaction coordinate is essentially related to the contraction of the B(5′)-B(10′) connectivity and the elongation of the B(2′)-B(5′) and B(1′)-B(10′) bond distances as shown in the Supporting Information, Figure S5.

The geometrical change profiles of T_1 and S_1 with respect to S_0 for **2** may be found as in the Supporting Information, Figures S2 and S3. As was the case for **1**,[3] the greatest changes in molecular geometry occur at the conical intersection crossing along the PEH of the S_1 state. At this point the calculated geometry loses its ground-state symmetry. Although the majority of the B-B and B-S connectivity distances for **2** at its $(S_0/S_1)_{CI}$ remain essentially unchanged from those distances at its S_0 ground state (Supporting Information, Figure S4), elongation of B(8)-B(9) ($|\Delta d| \sim 1.36$ Å) and B-B contraction for B(7)-B(8) distance ($\Delta d \sim 0.26$ Å) break the molecular C_i symmetry. The resulting deformation of the B(8)-B(4)-B(9) structural deltahedron also leads to disruption of the H(8,9) bridging hydrogen (3-center, 2-electron) bond and the establishment of a B-H bond at the B(9) position of terminal 2-center, 2-electron character. Additionally, the thiol group rotates, changing the dihedral angle ∠ B(1)-B(4)-SH through 80.2° from 9.8° to 90.0°.

The geometry corresponding to the ISC along the PEH of the T_1 state also has some notable changes when compared to the ground-state structure of **2** (Supporting Information, Figure S5). A contraction of about 0.21 Å for the B(5′)-B(10′) connectivity and elongations for B(2′)-B(5′) ($|\Delta d| \sim 0.49$ Å) and B(1′)-B(10′) ($|\Delta d| \sim 0.79$ Å) are the main geometrical variances. Finally, the dihedral angles ∠B(1)-B(4)-SH and ∠B(1′)-B(4′)-SH′ change from 9.8° to 20.2° and 29.7°, respectively.

■ CONCLUSION

We have demonstrated that the tuning of the fluorescent *anti*-$B_{18}H_{22}$ (**1**) cluster, by straightforward chemical substitution to produce 4,4′-$(HS)_2$-*anti*-$B_{18}H_{20}$ (**2**), facilitates ISC from excited singlet states to a triplet manifold. This subsequently enhances singlet oxygen production from a quantum yield of $\Phi_\Delta \sim 0.008$ in **1** to 0.59 in **2**. For the two isomers of $B_{18}H_{22}$, the S_1-T_1 energy gap is large at their S_1 minimum geometries and, although this gap considerably decreases at their CI regions,[3] the population of triplet manifolds at these points is inhibited by the relatively large energy barrier to the $(S_1/S_0)_{CI}$ crossing in the *anti* isomer, or the preference for ultrafast internal conversion at $(S_1/S_0)_{CI}$ for the *syn* isomer. Consequently ISC to triplet states do not significantly compete with fluorescence in **1** and internal conversion in *syn*-$B_{18}H_{22}$, thus explaining the low quantum yield of $O_2(^1\Delta_g)$ formation for these two isomers. However, in **2** the energy difference between S_1 and T_1 is a relatively small 0.14 eV, with a computed SOC of 3.37 cm^{-1} at the S_1 minimum, and 0.11 eV and SOC of 2.97 cm^{-1} at the FC region. $S_1 \rightarrow T_1$ ISC processes are therefore likely in these two regions of the PEH of **2**. The presence of molecular oxygen favors the production of O_2 $(^1\Delta_g)$ which usually proceeds through photosensitization from a triplet state of a donor system via an energy transfer process. Generally, the more efficiently the triplet state is populated, the larger is the coupling with the resulting singlet oxygen state, and the higher will be the $O_2(^1\Delta_g)$ production.[21]

The luminescence of **2** together with its ability to generate $O_2(^1\Delta_g)$ is a significant combination of properties that warrants a greater degree of investigation. Consequently, we are focusing our efforts on the investigation of the potential applications of these properties. One avenue we are pursuing is the self-assembly of **2** on gold or silver surfaces similar to that carried out for thiolated decaboranes.[15] Preliminary XPS results indicate a densely packed coverage of surfaces by monomolecular thiolate layers of {4-(S)-4′-(HS)-*anti*-$B_{18}H_{20}$}. Preliminary measurements of dynamic contact angles of water droplets show, with a high consistency, the increased hydrophilicity of these modified surfaces, thereby indicating a linear arrangement of {4-(S)-4′-(HS)-*anti*-$B_{18}H_{20}$} molecules away from the surface with the “free” −SH groups pointing outward from the surface. These modified surfaces have a potential to produce $O_2(^1\Delta_g)$, and we are interested to see to what degree the modified surface molecules can be probed by their fluorescence. In addition to the photophysical characteristics, the adsorbed $B_{18}H_{20}(SH)_2$ molecules have potential for further chemical reaction analogous to that found for $B_{10}H_{13}(SH)$ modified surfaces.[15] We are also pursuing the syntheses of alternative structural modifications to the fluorescent *anti*-$B_{18}H_{22}$, other than thiolation, that do not significantly alter the 18-vertex cluster architecture of the molecule, and yet enhance singlet−triplet transitions via *heavy atom perturbation*. In this regard we are investigating halogenated derivatives of compound **1** as well as substitutions with heavier elements such as selenium.

■ EXPERIMENTAL SECTION

General Procedures. Dried, deoxygenated solvents were stored over a suitable drying agent in evacuated flasks sealed with a high-vacuum Teflon stopcock. Reactions were carried out using standard Schlenk-line vacuum techniques although subsequent isolations were carried out in air. NMR spectroscopy was performed with a field of 7.1 T (corresponding to nominal 300 MHz ^{1}H frequency). Compound **1** was prepared as described previously.[5] All other chemicals were purchased commercially and used as delivered.

Synthesis of 4,4′-(HS)$_2$-*anti*-B$_{18}$H$_{20}$ (2). A thick-walled glass vessel, suitable for high-pressure experimentation, was charged, in a glovebox, with **1** (1.0 g, 4.6 mmol), $AlCl_3$ (6.2 g, 46.2 mmol), and elemental sulfur (1.5 g, 46.2 mmol), sealed with a vacuum tap attached to the vessel by a Tygon tube, removed from the glovebox and then flame-sealed under reduced pressure. The sealed contents of the glass vessel were then thoroughly shaken to ensure a homogeneous mixture of the reactants. The vessel was then immersed in an oil bath, and the temperature gradually increased to 125 °C. After 16 h at this temperature the contents formed a thick red-colored, very viscous, liquid that solidified on cooling. The reaction vessel was carefully removed from the hot oil bath and allowed to cool to room temperature. The vessel was then wrapped in aluminum foil and a towel and then carefully broken with the strike of a hammer (the reaction produces no gaseous product and therefore the controlled breakage of the glass vessel is quite safe). All the contents of the reaction vessel were then collected and washed several times with hot cyclohexane to remove any unreacted **1**. The remaining solid was then dissolved in distilled water (50 mL), to which was added dilute HCl (12%, 15 mL) and benzene (50 mL), and the mixture was allowed to stir for 30 min. The top benzene layer was separated, dried with anhydrous magnesium sulfate, filtered, and then reduced in volume until a yellow precipitate formed. This precipitate was dissolved in the minimum amount of boiling cyclohexane/benzene (9:1 by volume) and allowed to slowly cool to room temperature to form yellow/orange crystals of 4,4′-(HS)$_2$-*anti*-$B_{18}H_{20}$ (**2**) (1.03 g, 3.6 mmol, 80% yield). Melting pt. >400 °C. NMR data are listed in Table 3.

Single-Crystal X-ray Diffraction. Crystal data for 4,4′-(HS)$_2$-*anti*-$B_{18}H_{20}\cdot C_6H_6$: $C_6H_{28}B_{18}S_2$, M = 358.98, yellow bar, 0.5 × 0.3 × 0.2 mm^3, monoclinic, space group $C2/c$ (No. 15), a = 18.6632(5), b = 10.4904(2), c = 10.7580(3) Å, β = 99.2149(12)°, V = 2079.07(9) Å^3, Z = 4, D_c = 1.147 g/cm^3, F_{000} = 744, Nonius KappaCCD area detector, MoKα radiation, λ = 0.71073 Å, T = 150(2) K, $2\theta_{max}$ = 55.0°, 24174 reflections collected, 2383 unique (R_{int} = 0.030). The structure was solved and refined using the programs SIR92 and SHELXL-97 respectively.[6] The program X-Seed[7] was used as an interface to the SHELX programs, and to prepare the figures. Final GoF = 1.062, $R1$ = 0.0315, $wR2$ = 0.0937, R indices based on 2103 reflections with $I > 2\sigma(I)$ (refinement on F^2), 159 parameters, 0 restraints. Lp and absorption corrections applied,μ = 0.244 mm^{-1}. Crystal structure data compound **2** has been deposited at the Cambridge Crystallographic Data Centre and allocated the deposition number CCDC 912917.

Theoretical Methodology. Both DFT and ab initio CASSCF/CASPT2 methods[8] were used to compute PEH minima and crossings, together with state and transition properties for the lowest-lying singlet and triplet states of 4,4′-(HS)$_2$-*anti*-$B_{18}H_{20}$ isomer as explained elsewhere.[3] The ground S_0 and low-lying triplet T_1 state minima were optimized at the DFT/B3LYP/6−31+G* level,[9] whereas the other PEH minima and crossings geometry optimizations were performed at the CASSCF level. The active space consists of 12 electrons correlated into 12 molecular orbitals, CASSCF(12/12) hereafter. The vertical energy calculations have been computed by using the CASPT2 method employing as reference the CASSCF(12/12) wave function. The conical intersection structures have been determined as minimum energy crossing points (MECP)[10] between the two states involved. The one-electron atomic basis set 6−31+G* has been used throughout. Symmetry constraints have been imposed in all computed minima, but no symmetry restrictions have been enforced during crossing calculations. C_i symmetry for **2** has been employed in the computation of minima, therefore the corresponding state labeling will be used when required. Oscillator strengths and radiative lifetimes have been determined from the computed CASSCF transition dipole moments (TDM) and the CASPT2 excitation energies. The radiative lifetimes have been obtained for the low-energy excited singlet and triplet states using the Strickler−Berg relationship, valid under the assumption that excited state nonradiative deactivation is of minor importance. Spin−orbit coupling (SOC) terms between singlet and triplet states have been computed within the AMFI and CASSI frameworks.[11] Calculations have been performed with Gaussian 09[12] (DFT) and MOLCAS-7[13] (CASSCF/CASPT2) sets of programs. The former has also been used for the C_i-symmetry constrained B3LYP/6−31+G* geometry optimization (found as a minimum on the respective PEH as revealed by the second derivative analysis) and for magnetic properties computations with a TZP basis set by Huzinaga (denoted as II), which is well-designed for such types of computations. [Huzinaga, S. *Approximate Atomic Wave Functions*; University of Alberta, Edmonton, Canada, **1971**] Additional data for the optimized geometries are specified in the Supporting Information.

Photophysical Experimental Techniques. *Transient Absorption and Time-Resolved Phosphorescence.* The samples in cyclohexane were excited with a Lambda Physik COMPEX 102 excimer laser (308 nm, pulse width 28 ns), and the corresponding spectra were measured within 350−800 nm on a laser kinetic spectrometer LKS 20 (Applied Photophysics, U.K.). The time profiles of the transients were recorded using a 150 W Xe lamp (Phillips) equipped with a pulse unit and a R928 photomultiplier (Hamamatsu).

The time-resolved near-infrared luminescence of $O_2(^1\Delta_g)$ at 1270 nm was monitored using a Ge detector upon laser excitation at 308 nm. The signal from the detector was collected on a 600 MHz Agilent Infiniium oscilloscope and transferred to a computer for further analysis. The signal-to-noise ratio of the signals was improved by the averaging of 100 individual traces. The short-lived signal produced by the scattering of an excitation laser pulse was eliminated by exciting the argon-saturated sample and subtracting the obtained signal from the signal recorded in oxygen or air atmosphere. The quantum yields of singlet oxygen formation, Φ_Δ, were estimated by the comparative method using 5,10,15,20-tetraphenylporphyrin (TPP) as a standard ($\Phi_\Delta = 0.67$ in cyclohexane).[14]

Fluorescence Spectroscopy. The steady-state and time-resolved fluorescence were monitored using a Horiba Jobin Yvon Fluorolog 3 spectrometer. Fluorescence lifetime measurements were performed using a laser-diode excitation at 405 nm (NanoLED-405LH, pulse width 750 ps, repetition rate 1 MHz). The emission was recorded using a cooled TBX-05-C photon detection module in a time-correlated single-photon counting regime. The decay curves were fitted to exponential functions using the iterative reconvolution procedure of the DAS6 software (v. 6.4, Horiba Jobin Yvon, 2009).

■ ASSOCIATED CONTENT

Ⓢ Supporting Information

Additional information includes a filmed melting-point experiment for **2**. Samples of the compound were heated at a rate of 10 °C min^{-1} in an inert argon atmosphere up to a maximum of 400 °C. Additional computational details; theoretical (CASPT2) and experimental absorption spectra of **2**; Cartesian coordinates (Å) of the crystallographic structure of **2** and of the DFT/B3LYP and CASSCF(12/12) optimized structures, and CASSCF(12/12) absolute energies for the corresponding state 6−31+G* basis set. Boron-boron and boron-sulfur distance differences (Å) between the geometries of the ground state S_0 optimized at the DFT/B3LYP level and the crystal structure of **2** (C_i symmetry). Boron-boron and boron-sulfur distance differences (Å) between the minimum energy geometries of the ground state S_0 and the following: (1) the lowest singlet excited state S_1 in **2**, (2) the lowest triplet excited state T_1 in **2**, (3) the conical intersection geometry $(S_0/S_1)_{CI}$ in **2**, and (4) the ISC geometry $(S_0/T_1)_{ISC}$ in **2**. Comparison of time-resolved absorption of the triplet states of **2**. This material is available free of charge via the Internet at http://pubs.acs.org.

■ AUTHOR INFORMATION

Corresponding Author

*E-mail: michaell@iic.cas.cz (M.G.S.L.), lang@iic.cas.cz (K.L.), j.m.oliva@iqfr.csic.es (J.M.O.).

Notes

The authors declare no competing financial interest.

■ ACKNOWLEDGMENTS

We gratefully acknowledge the support of the Czech Science Foundation (Grant nos. P207/11/1577 and P208/10/1678) and of projects CTQ2010-14892, and CSD2007-0010 Consolider-Ingenio in Molecular Nanoscience of the Spanish MICINN/FEDER. The services and computer time made available by the Servei d'Informàtica de la Universitat de València are also acknowledged. We would also like to thank Zdeňka Kolská Ph.D. and her parent institute for her work conducted on determining the melting-point of compound **2**.

■ REFERENCES

(1) (a) Kawasaki, Y.; Kuroi, T.; Yamashita, T.; Horita, K.; Hayashi, T.; Ishibashi, M.; Togawa, M.; Ohno, Y.; Yoneda, M.; Horsky, T.; Jacobson, D.; Krull, W. *Nucl. Instrum. Meth. B* **2005**, *237*, 25. (b) Harris, M. A.; Huynh, C. *Solid State Technol.* **2007**, *50*, 33. (c) Marques, L. A.; Pelaz, L.; Santos, I.; Venezia, V. C. *Phys. Rev. B* **2006**, *74*, 201201. (d) Kawasaki, Y.; Shibahara, K. J. *Vac. Sci. Technol.* **2012**, *30*, 011601.

(2) Londesborough, M. G. S.; Bould, J.; Baše, T.; Hnyk, D.; Bakardjiev, M.; Holub, J.; Císařová, I.; Kennedy, J. D. *Inorg. Chem.* **2010**, *49*, 4092.

(3) Londesborough, M. G. S.; Hnyk, D.; Bould, J.; Serrano-Andres, L.; Sauri, V.; Oliva, J. M.; Kubat, P.; Polivka, T.; Lang, K. *Inorg. Chem.* **2012**, *51*, 1471.

(4) Volkov, V. V.; Il'inchik, E. A.; Volkov, O. V.; Yuryeva, O. O. *Chem. Sustainable Dev.* **2000**, *8*, 185.

(5) Pitochelli, A. R.; Hawthorne, M. F. *J. Am. Chem. Soc.* **1962**, *84*, 3218.

(6) (a) Altomare, A.; Cascarano, G.; Giacovazzo, C.; Guagliardi, A.; Burla, M. C.; Polidori, G.; Camalli, M. *J. Appl. Crystallogr.* **1994**, *27*, 435. (b) Sheldrick, G. *Acta Crystallogr., Sect. A* **2008**, *64*, 112.

(7) Barbour, L. J. *J. Supramol. Chem.* **2001**, *1*, 189.

(8) (a) Roos, B. O.; Andersson, K.; Fulscher, M. P.; Malmqvist, P. A.; Serrano-Andrés, L.; Pierloot, K.; Merchán, M. *Adv. Chem. Phys.* **1996**, *93*, 219. (b) Andersson, K.; Malmqvist, P. A.; Roos, B. O. *J. Chem. Phys.* **1992**, *96*, 1218. (c) Andersson, K.; Malmqvist, P. A.; Roos, B. O.; Sadlej, A. J.; Wolinski, K. *J. Phys. Chem.* **1990**, *94*, 5483.

(9) (a) Lee, C.; Yang, W.; Parr, R. G. *Phys. Rev. B* **1988**, *37*, 785. (b) Becke, A. D.. *J. Chem. Phys.* **1993**, *98*, 5648.

(10) Serrano-Andrés, L.; Merchán, M.; Lindh, R. *J. Chem. Phys.* **2005**, *122*, 104107.

(11) (a) Rubio-Pons, O.; Serrano-Andrés, L.; Merchán, M. *J. Phys. Chem. A* **2001**, *105*, 9664. (b) Strickler, S. J.; Berg, R. A. *J. Chem. Phys.* **1962**, *37*, 814.

(12) Frisch, M. J.; Trucks, G. W.; Schlegel, H. B.; Scuseria, G. E.; Robb, M. A.; Cheeseman, J. R.; Scalmani, G.; Barone, V.; Mennucci, B.; Petersson, G. A.; Nakatsuji, H.; Caricato, M.; Li, X.; Hratchian, H. P.; Izmaylov, A. F.; Bloino, J.; Zheng, G.; Sonnenberg, J. L.; Hada, M.; Ehara, M.; Toyota, K.; Fukuda, R.; Hasegawa, J.; Ishida, M.; Nakajima, T.; Honda, Y.; Kitao, O.; Nakai, H.; Vreven, T.; Montgomery, J. A.; , Jr., Peralta, J. E.; Ogliaro, F.; Bearpark, M.; Heyd, J. J.; Brothers, E.; Kudin, K. N.; Staroverov, V. N.; Kobayashi, R.; Normand, J.; Raghavachari, K.; Rendell, A.; Burant, J. C.; Iyengar, S. S.; Tomasi, J.; Cossi, M.; Rega, N.; Millam, J. M.; Klene, M.; Knox, J. E.; Cross, J. B.; Bakken, V.; Adamo, C.; Jaramillo, J.; Gomperts, R.; Stratmann, R. E.; Yazyev, O.; Austin, A. J.; Cammi, R.; Pomelli, C.; Ochterski, J. W.; Martin, R. L.; Morokuma, K.; Zakrzewski, V. G.; Voth, G. A.; Salvador, P.; Dannenberg, J. J.; Dapprich, S.; Daniels, A. D.; Ö. Farkas, Foresman, J. B.; Ortiz, J. V.; Cioslowski, J.; Fox, D. J.; Pople, J. A. *Gaussian 09* (Revision A.1); Gaussian, Inc: Wallingford, CT, 2009.

(13) Aquilante, F.; De Vico, L.; Ferré, N.; Ghigo, G.; Malmqvist, P. A.; Neogrady, P.; Pedersen, T. B.; Pitonak, M.; Reiher, M.; Roos, B. O.; Serrano-Andres, L.; Urban, M.; Veryazov, V.; Lindh, R. *J. Comput. Chem.* **2010**, *31*, 224.

(14) Schmidt, R.; Afshari, E. *J. Phys. Chem.* **1990**, *94*, 4377.

(15) Bould, J.; Macháček, J.; Londesborough, M. G. S.; Macías, R.; Kennedy, J. D.; Bastl, Z.; Rupper, P.; Baše, T. *Inorg. Chem.* **2012**, *51*, 1685.

(16) Li, H.; Min, D.; Shore, S. G.; Lipscomb, W. N.; Yang, W. *Inorg. Chem.* **2007**, *46*, 3956.

(17) Gibb, T. C.; Kennedy, J. D. *J. Chem. Soc., Faraday Trans.* **1982**, *78*, 525.

(18) Hamilton, E. J. M.; Kultyshev, R. G.; Du, B.; Meyers, E. A.; Liu, S.; Hadad, C. M.; Shore, S. G. *Chem.—Eur. J.* **2006**, *12*, 2571.

(19) Fontaine, X. L. R.; Greenwood, N. N.; Kennedy, J. D.; MacKinnon, P. *J. Chem. Soc., Dalton Trans.* **1988**, 1785.

(20) Heřmanek, S. *Chem. Rev.* **1992**, *92*, 325.

(21) Serrano-Pérez, J. J.; Olaso-González, G.; Merchán, M.; Serrano-Andrés, L. *Chem. Phys.* **2009**, *360*, 85.

(22) Lang, K.; Mosinger, J.; Wagnerová, D. M. *Coord. Chem. Rev.* **2004**, *248*, 321−350.

(23) Frutos, L. M.; Castano, O. *J. Chem. Phys.* **2005**, *123*, 104108.

(24) (a) Carr, M. J.; Clegg, W.; Kennedy, J. D.; Londesborough, M. G. S.; Kilner, C. A. *Collect. Czech. Chem. Commun.* **2010**, *75*, 807. (b) Jelínek, T.; Císařová, I.; Štíbr, B.; Kennedy, J. D. *Dalton Trans.* **2007**, *42*, 4766. (c) Shea, S. L.; Jelínek, T.; Perera, S. D.; Štíbr, B.; Thornton-Pett, M.; Kennedy, J. D. *Dalton Trans.* **2004**, *10*, 1521. (d) Dosangh, P. K.; Bould, J.; Londesborough, M. G. S.; Jelínek, T.; Thornton-Pett, M.; Štíbr, B.; Kennedy, J. D. *Organometallic Chem.* **2003**, *680*, 312.

(25) Wilkinson, F.; Helman, W. P.; Ross, A. B. *J. Phys. Chem. Ref. Data* **1995**, *24* (2), 663.